The Journal of Experimental Biology 210, 2969-2978
Published by The Company of Biologists 2007
doi:10.1242/jeb.005942

Analytical and numerical investigation of the flow past the lateral antennular flagellum of the crayfish *Procambarus clarkii*

Joseph A. C. Humphrey[1,2,*] and DeForest Mellon, Jr[1]

[1]*Department of Biology and* [2]*Department of Mechanical and Aerospace Engineering, University of Virginia, Charlottesville, VA 22904, USA*

*Author for correspondence (e-mail: jach@virginia.edu)

Accepted 11 June 2007

Summary

Analytical and numerical methodologies are combined to investigate the flow fields that approach and pass around the lateral flagellum of the crayfish *Procambarus clarkii*. Two cases are considered, the first being that of a free-flicking flagellum and the second corresponding to a flagellum fixed inside a small bore tube. The first case is the natural one while the second corresponds to the experimental configuration investigated by Mellon and Humphrey in the accompanying paper. In that study the authors observed a hydrodynamic-dependent asymmetry in the spiking responses recorded from single, bimodally sensitive local interneurons (Type I) in the crayfish deutocerebrum, whereby the direction of an abruptly initiated flow of freshwater (or odorant) past the flagellum resulted in consistently larger numbers of spikes in response to the hydrodynamic stimulation when the flow direction was proximal-to-distal. In this communication we show that the proximal-to-distal and the distal-to-proximal flows produced in the flagellum-in-tube experiment correspond closely to the flows associated with the downward and upward flicks, respectively, of a free-flicking flagellum. We also show from calculations of the drag forces acting on the putative mechanoreceptor sensilla circumferentially distributed around a free-flicking flagellum that there are at least three sources of hydrodynamic asymmetry possibly related to the electrophysiological asymmetry observed: (i) the sense of the drag forces acting on medial and lateral mechanoreceptors changes in the same way for both with change in flick direction; (ii) during a downward (an upward) flick, a ventral (dorsal) mechanoreceptor experiences a larger drag force magnitude than a dorsal (ventral) mechanoreceptor; (iii) because of the difference in speeds between downward and upward flicks, the magnitudes of the drag forces acting on medial, lateral and ventral mechanoreceptors during a downward flick are about two times larger relative to the forces acting on medial, lateral and dorsal mechanoreceptors during an upward flick. All three of these naturally occurring hydrodynamic asymmetries are correctly reproduced in the flagellum-in-tube experiment.

Key words: crustacean, hydrodynamics, mathematical analysis.

Introduction

The main purpose of this theoretical modeling effort is to establish and compare the flow fields arising around a free-flicking flagellum and around a flagellum fixed in a small diameter tube. The free-flicking flagellum corresponds to the natural situation and, therefore, its analysis should be of broad interest. The analysis of the flagellum-in-tube case serves to validate and further clarify the experimental conditions of the investigation reported in the accompanying paper (Mellon and Humphrey, 2007). In that study the authors observed a hydrodynamic-dependent asymmetry in the spiking responses recorded from single, bimodally sensitive local interneurons (Type I) in the crayfish deutocerebrum. Specifically, they found that in an abruptly initiated flow of water (or odorant) past the flagellum, consistently larger numbers of spikes were recorded in response to the hydrodynamic stimulation when the flow direction was proximal-to-distal. Among other things, in this communication we show that the proximal-to-distal and the distal-to-proximal flows produced in the flagellum-in-tube experiment correspond closely to the downward and upward flicks, respectively, of a free-flicking flagellum.

The putative mechanoreceptors of interest are beak-shaped sensilla distributed circumferentially and along the length of the flagellum. We show from calculations of the drag forces acting on them for free-flicking conditions that there are at least three sources of hydrodynamic asymmetry possibly related to the electrophysiological asymmetry: (i) the sense of the drag forces acting on medial and lateral mechanoreceptors changes in the same way for both with change in flick direction; (ii) during a downward (an upward) flick, a ventral (dorsal) mechanoreceptor experiences a larger drag force magnitude than a dorsal (ventral) mechanoreceptor; (iii) because of the difference in speeds between downward and upward flicks, the magnitudes of the drag forces acting on medial, lateral and ventral mechanoreceptors during a downward flick are about

two times larger relative to the forces acting on medial, lateral and dorsal mechanoreceptors during an upward flick.

By necessity, the analyses presented here are based on simplified geometrical models for the two flagellum flow configurations considered. However, they are guided by kinematic observations and all the essential physics is retained in order to ensure that: (i) the free-flicking flagellum results are generally applicable and of broad interest; (ii) a comparison between the free-flicking and flagellum-in-tube results is helpful for interpreting the electrophysiological findings of Mellon and Humphrey (Mellon and Humphrey, 2007). In this sense especially, the analyses strongly complement the electrophysiological work, since it would be very challenging and require considerable effort and time to perform comparable velocity measurements for the two flagellum flow configurations.

Methods, Results and Discussion

Analytical and numerical modeling considerations

This section of the paper covers five interrelated theoretical topics. For each topic we present the relevant methodology followed by pertinent results and their discussion. The topics are as follows. (1) Analysis of the kinematics of the flows approaching a downward and upward flicking flagellum, respectively. (2) Analysis of the kinematics of the flow approaching the aesthetascs and putative mechanoreceptor sensilla on a downward flicking flagellum. (3) Numerical calculation of the dynamics of the flow around a downward or upward flicking flagellum. (4) Numerical calculation of the dynamics of the flow around a flagellum in a tube. (5) Numerical calculation of the drag forces and torques acting on the hydrodynamic mechanoreceptor sensilla of free-flicking and tube flow flagella, respectively.

(1) Kinematics of the flows approaching a downward and upward flicking flagellum

The geometry of an idealized flagellum shown flicking downwards in quiescent water is sketched in Fig. 1 relative to an (*X*–*Y*) coordinate system (frame of reference) fixed on the rotation pivot point. Our kinematic observations show that a downward flicking flagellum deflects by an angle of approximately 15° in 0.05 s, corresponding to an angular velocity of 5.24 rad s^{-1}, and that the downward/upward flick velocity ratio is 1.66, approximately. The fluid drag forces acting on the deformable flagellum determine its final equilibrium shape during the downward and upward flicks, respectively. We find that these shapes are acquired very early in a stroke for either flick direction, and that they are retained throughout the remaining motion of the flick. During the downward flick the flagellum curves by as much as 40°, approximately, along the distal third of its length relative to the proximal two thirds, which remains essentially straight. During the upward flick the flagellum is essentially straight along its entire length.

At any arc location, z, along the flagellum, starting from its base, we define an (*x*–*y*) coordinate system, with the x coordinate aligned along the secant, $R(z)$, connecting the pivot point and point z, and with the y coordinate aligned normal to $R(z)$. By construction, the vector velocity of the water approaching the flagellum, $\vec{U}_{yf}$, relative to the (*x*–*y*) coordinate system fixed at z, is aligned along the y coordinate. Call γ the angle formed by the x-coordinate and the tangent, t_f, to the flagellum at point z. Then, also from construction, the approaching velocity components normal and tangent to the flagellum at point z are given by $U_{nf}=U_{yf}\cos\gamma$ and $U_{tf}=U_{yf}\sin\gamma$, where U_{yf} is the magnitude of $\vec{U}_{yf}$. The ratio of these two velocity components is given by $U_{tf}/U_{nf}=\tan\gamma$. During a downward flick the angle γ is very small along the proximal two thirds of the flagellum but increases to values of the order 40° along the distal third, towards the flagellum tip. Thus, for a downward flick we expect U_{tf}/U_{nf} to be close to zero along the proximal two thirds of the flagellum and to vary from 0 to 0.84, approximately, along the distal third. During an upward flick the flagellum is essentially straight so that U_{tf}/U_{nf} is very close to zero along its entire length. The conclusions are that: (i) the approaching velocity component tangent to a downward flicking flagellum is always positive, directed from base to tip along its distal third, as sketched in Fig. 1; (ii) along the proximal two thirds of a downward flicking flagellum, the magnitude of the velocity component normal to it significantly exceeds the tangential component, whereas along the distal third the two velocity components gradually become comparable in magnitude; (iii) for an upward flicking flagellum the magnitude of the velocity component normal to it significantly exceeds the tangential component everywhere along its length.

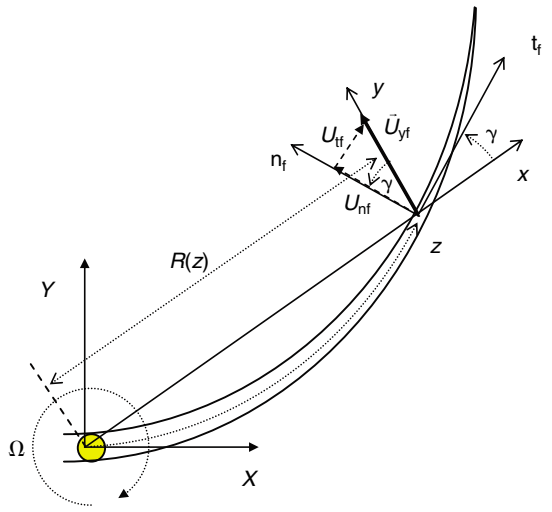

Fig. 1. Schematic of a downward flicking flagellum rotating at angular velocity Ω relative to the pivot point at its base in a fixed *X*–*Y* coordinate system. Relative to an *x*–*y* coordinate system fixed at point z along the flagellum's arc length, the approaching local fluid velocity normal to the secant $R(z)$ is U_{yf}. This generates components $U_{nf}=U_{yf}\cos\gamma$ and $U_{tf}=U_{yf}\sin\gamma$ along the normal (n_f) and tangent (t_f) to the flagellum. Aesthetascs and hydrodynamic sensilla on the flagellum are not shown.

(2) Kinematics of the flow approaching the aesthetascs and putative mechanoreceptor sensilla on a downward flicking flagellum

Fig. 2 is a sketch of an idealized aesthetasc or beak-shaped mechanoreceptor sensillum attached to a point z on the ventral side of the curved, downward flicking flagellum shown in Fig. 1.

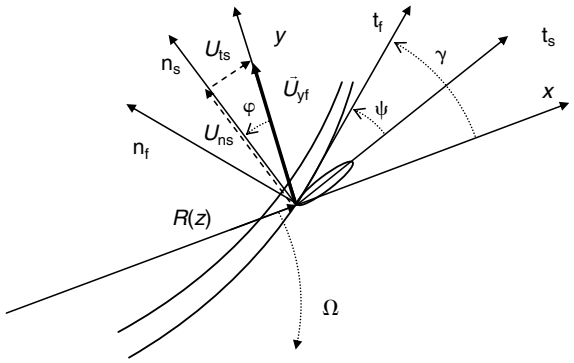

Fig. 2. Schematic of an aesthetasc or mechanoreceptor sensillum on a downward flicking flagellum rotating at angular velocity Ω relative to its base (see Fig. 1). The fluid velocity approaching the flagellum, U_{yf}, generates components $U_{ns}=U_{yf}\cos\varphi$ and $U_{ts}=U_{yf}\sin\varphi$ along the normal (n_s) and tangent (t_s) to the sensillum, where $\varphi=\gamma-\psi$.

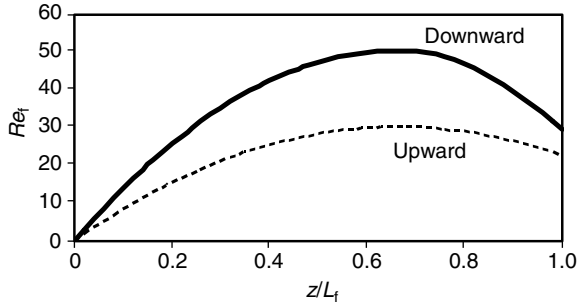

Fig. 3. Variation of the Reynolds number Re_f along the dimensionless length of a flicking flagellum for downward (Ω=5.24 rad s^{-1}) and upward (Ω=3.14 rad s^{-1}) flicks; flagellum dimensions are given in the text. The decreases in flagellum diameter and of the normal component of velocity with increasing distance toward the flagellum tip account for the reduction in Re_f with increasing z/L_f.

Relative to an (x–y) coordinate system (as defined in Fig. 1) fixed at the base of the sensillum, the vector velocity of the water approaching it, $\vec{U}_{yf}$, can be decomposed to define the velocity components normal and tangent to the sensillum. These two quantities are given by $U_{ns}=U_{yf}\cos\varphi$ and $U_{ts}=U_{yf}\sin\varphi$, respectively, where $\varphi=\gamma-\psi$ and γ is as defined in Fig. 1. We know for both the aesthetascs and the putative mechanoreceptors that $\psi\cong45°$, and that $\gamma\cong0°$ along the proximal two thirds of the flagellum and $0°\leqslant\gamma\leqslant40°$ along the distal third. It follows that $\varphi\cong-45°$ along the proximal two thirds of the flagellum and $-45°\leqslant\varphi\leqslant-5°$ along the distal third. As a consequence, the ratio of the two velocity components, $U_{ts}/U_{ns}=\tan\varphi$, is close to –1 along the proximal two thirds of the flagellum and ranges from –1 to –0.09, approximately, along the distal third. The conclusions are that: (i) the approaching velocity component tangent to an aesthetasc or a mechanoreceptor on the ventral side of a downward flicking flagellum is always negative, directed from sensillum tip to base, contrary to the sense of motion assumed for analysis in Fig. 2; (ii) the magnitudes of the two velocity components approaching these sensilla are comparable along the proximal two thirds of the flagellum, whereas along the distal third the normal velocity component gradually exceeds the tangential significantly.

Medially and laterally located mechanoreceptors also have inclination angles $\psi\cong45°$ with respect to the local flagellum surface. However, because they are oriented in the direction of the local tangent to the flagellum, t_f, these sensilla experience the same approaching velocity components as the flagellum itself, meaning that $U_{ns}=U_{nf}$ and $U_{ts}=U_{tf}$ for both downward and upward flicking motions. Because of the recirculating nature of the flow that arises in the wake of a downward (upward) flicking flagellum, an analysis of the velocity components approaching mechanoreceptor sensilla on the dorsal (ventral) side of the flagellum must await more detailed numerical calculations, presented below.

(3) Dynamics of the flow around a downward or upward flicking flagellum

A flicking flagellum can be approximated as a curved, slender, cone-like object of length L_f and of diameter d_f at location z along its length such that $L_f/d_f\gg1$ anywhere along the flagellum. The cross-section of a flagellum has the shape of a distorted (egg-like) ellipse with its minor/major semi-axes in the ratio of b/a=0.67, approximately, at any location z along the flagellum. We can define an effective flagellum diameter as $d_f=(2a+2b)/2=1.667a$, whose z dependence is given by $d_f=d_b-[(d_b-d_t)/L_f]z$, where d_b and d_t are the effective base and tip diameters, respectively. In this study for a flicking flagellum we take $d_b\cong1$ mm, $d_t\cong0.25$ mm, and L_f=25 mm, from which it follows that the cone angle is 3.4°.

At any location z along the length of a flicking flagellum it is possible to define a Reynolds number (Re_f) based on the velocity component U_{nf}, approaching it normally as defined above relative to a coordinate system attached to the flagellum. Thus $Re_f\equiv\rho d_f U_{nf}/\mu$, where ρ (=996 kg m^{-3}) and μ ($=8.6\times10^{-4}$ kg m^{-1} s^{-1}) are the density and dynamic viscosity of water at 25°C, respectively. The normal component of velocity is given by $U_{nf}=U_{yf}\cos\gamma$ where, from Fig. 1, $U_{yf}=\Omega R(z)$, and $\Omega\approx5.24$ rad s^{-1} for a downward flick and $\Omega\approx3.14$ rad s^{-1} for an upward flick. Along the proximal two thirds of a downward flicking flagellum $\gamma\cong0°$, and along the remaining distal one third we assume to a good approximation that γ increases linearly with distance z, from 0° to 40°. In contrast, an upward flicking flagellum is essentially straight. The resulting distributions of Re_f as a function of dimensionless flagellum length are shown in Fig. 3. For both flick directions Re_f initially increases with z/L_f. However, because d_f decreases distally, Re_f eventually maximizes at a value of 50 at z/L_f=0.66 for a downward flick and at a value of 30, also at z/L_f=0.66, for an upward flick. For larger values of z/L_f the value of Re_f decreases relatively quickly because both d_f and U_{nf} decrease distally.

In the length range $0\leqslant z/L_f\leqslant0.75$, for which $0°\leqslant\gamma\leqslant8°$, the flow field around a downward flicking flagellum is predominantly two dimensional (2D) and the above definition of Re_f applies. With reference to Fig. 5, discussed further below, relative to an (x, y, z) Cartesian coordinate system fixed to the flagellum and with its z axis coinciding with the z axis of the flagellum, this 2D flow is contained in a plane normal to the z axis and consists of streamwise (U_x) and transverse (U_y) velocity components driven by the approaching normal velocity

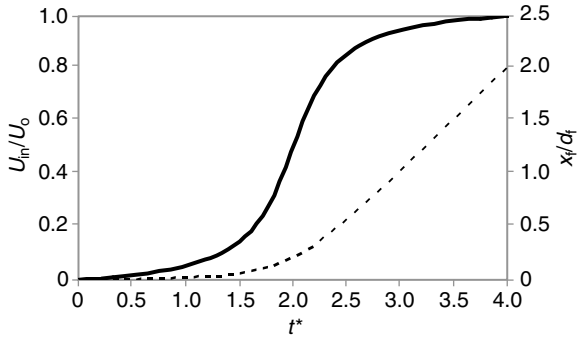

Fig. 4. S-shaped form of the dimensionless velocity (U_{in}/U_o, continuous line) approximating the rate of acceleration of the far-field flow approaching a flicking flagellum as a function of dimensionless time, t^* ($\equiv tU_o/d_f$). (In the calculations the flagellum is fixed and the flow accelerates past it.) Also shown is the dimensionless distance (x_f/d_f, broken line) traveled by the approaching flow in units of the flagellum diameter. For the conditions of interest in this work, U_o=8.63×10^{-2} m s^{-1} and d_f=5×10^{-4} m.

component, U_{nf}, of the flow[1]. To elucidate this flow field, numerical calculations were performed for the transient, developing, 2D motion of water past a circular cylinder ultimately attaining a value of Re_f=50. This flow condition closely corresponds to the transient flow around a downward-flicking flagellum in the region $0.50 \leqslant z/L_f \leqslant 0.75$ and exactly corresponds to it for z/L_f=0.66. In addition, because of the closeness of the Reynolds numbers, the flow field calculated for Re_f=50 provides a fair representation of that arising around an upward-flicking flagellum for Re_f=30 (Tritton, 1988). The calculations were performed using the Flow and Heat Transfer Solver (FAHTSO) code developed by Rosales et al. (Rosales et al., 2000; Rosales et al., 2001), extended to include the Immersed Boundary technique (Pillapakkam et al., 2007). In this approach, curved surfaces are approximated on a Cartesian grid to allow the calculations to be performed in Cartesian coordinates. FAHTSO solves the full forms of the Navier–Stokes equations for constant property flows. Details regarding the code and its testing and applications are given in the above three references.

Because of the invariance of the incompressible-flow equations under unsteady motion (Panton, 1996), rather than solve for the flow field generated by a flagellum (cylinder) accelerating through water, we solve for the flow field of water accelerating past a fixed flagellum (cylinder). The 2D domain employed for the numerical calculations was $20d_f \times 20d_f$ units and the cylinder center was located at (x=5d_f, y=10d_f). Checks were conducted to ensure that the locations of the four domain boundaries were sufficiently removed from the cylinder so as not to adversely affect the calculated results. The boundary conditions employed were: (i) zero velocity at the cylinder surface; (ii) unidirectional, uniform flow with velocity $U_{in}=U_o$ ($\equiv U_{nf}$)[2] aligned in the x-coordinate direction at the inlet plane (x=0); (iii) developed flow at the outlet plane (x=20d_f); (iv) impermeable bottom (y=0) and top (y=20d_f) domain surfaces sliding at the inlet flow velocity U_o. For the calculations presented here the (x,y) grid consisted of (400×400) nodes and was unevenly spaced, being more refined near the cylinder surface to resolve the boundary layer forming on it. The dimensionless calculation time step was set to Δt^*=5.363×10^{-4}, where $t^* \equiv tU_o/d_f$, and at each time step the entire flow field was calculated according to an iterative scheme until it had converged within that time step.

The calculations were started with the water initially at rest. The flow at the inlet plane as well as the top and bottom domain boundaries was then accelerated according to an S-shaped curve given by:

$$U_{in} = U_o \frac{\arctan\left[\frac{2\pi}{T_p}\left(\frac{t^*}{t_f^*} - \frac{1}{2}\right)\right] + \mathrm{ABS}\left[\arctan\left(-\frac{\pi}{2}\right)\right]}{2\mathrm{ABS}\left[\arctan\left(-\frac{\pi}{2}\right)\right]}, \quad (1)$$

where t^* is dimensionless time, t_f^* is dimensionless final time, and T_p is an adjustable dimensionless constant that changes the slope of the S-shaped curve. The curve used, plotted in Fig. 4 and corresponding to T_p=0.5 and t_f^*=4, shows that by t^*=4 the flow field has acquired its final steady state velocity. Thus, in this calculation, by the time a flicking flagellum translates two body diameters it has essentially acquired its final steady state velocity, a condition closely matching our laboratory observations. Fig. 4 also shows as a function of time the dimensionless distance (x_f/d_f) traveled by the approaching flow past a fixed flagellum or, equivalently, the distance traveled by a flagellum moving through still water.

Values of d_f=5×10^{-4} m and U_o=8.63×10^{-2} m s^{-1} were set numerically to give the final developed flow value of Re_f=50 of interest to this work using water as the fluid medium. This value of d_f corresponds to the effective diameter of a 25 mm flagellum two thirds along its length starting from the base. However, note that, in dimensionless form, the calculated velocity results correspond to any (d_f, U_o) pair ultimately yielding Re_f=50 and, because $t^* \equiv tU_o/d_f$, in the t^* range explored other (d_f, U_o) pairs will correspond to different physical times, t.

As shown in Fig. 5, the developing flow around a downward-flicking flagellum ultimately attaining a value of Re_f=50 is laminar and streamlined. In the plots the streamlines are color-coded to indicate the local dimensionless magnitude of velocity ($U_{mag}/U_o = \sqrt{U_x^2 + U_y^2}/U_o$). Results are plotted for four dimensionless times t^*=1, 2, 3 and 4, corresponding to physical times of t=5.79×10^{-3} s, 1.16×10^{-2} s, 1.74×10^{-2} s and 2.32×10^{-2} s. The plots show the flow accelerating with time, especially where it curves near to and around the flagellum surface. A stagnation flow region arises immediately ahead of the flagellum, and a recirculating wake region consisting of two counter-rotating vortices grows with time immediately behind it. The flow in the vicinity of the stagnation point is characterized by a boundary layer of thickness $\delta/d_f = 1.2Re_f^{-1/2}$, approximately, that increases in thickness with distance traveled around the flagellum (Panton, 1996). Inertial and viscous fluid forces are comparable in magnitude in the boundary layer,

[1]Note that the (x, y, z) coordinate system used to describe the 2D flow around a flagellum is distinct and different from the (x, y, z) coordinate system used in Figs 1 and 2 for the kinematic analyses.

[2]In the context of the present analysis, the inlet velocity U_{in} is given the value U_o and corresponds to U_{nf}, the approaching velocity normal to the flagellum.

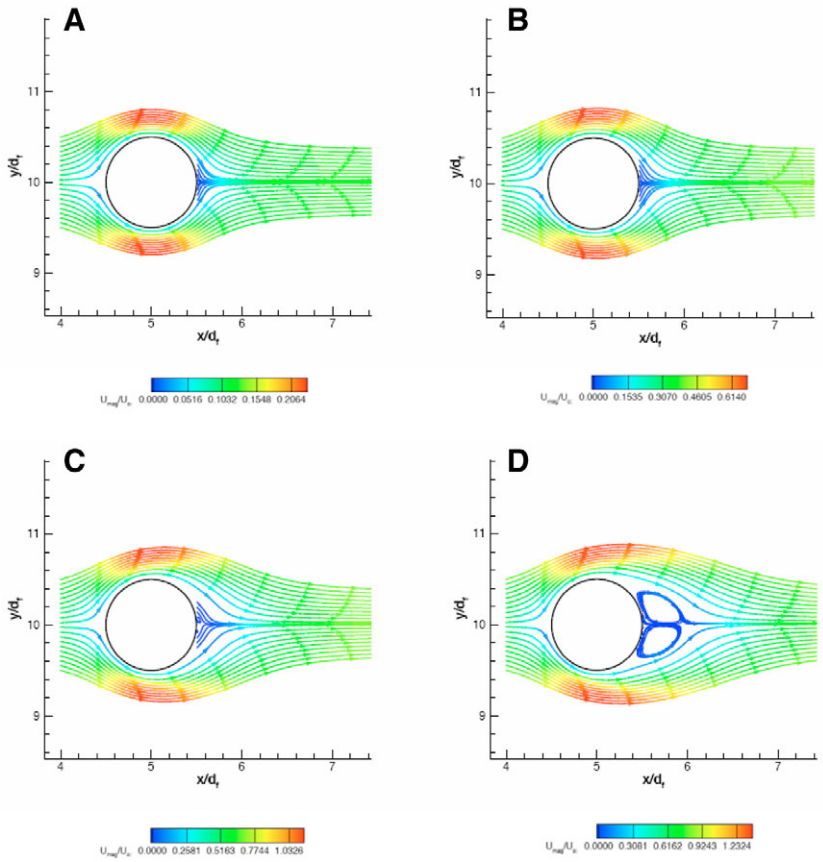

Fig. 5. Near-field flow streamlines with dimensionless velocity magnitude superimposed for the 2D flow accelerating (from left to right) past a flagellum (approximated as a long cylinder) according to the far field approaching velocity S-curve plotted in Fig. 4. Results are shown at times t^*=1 (A; Re_f=2.6), t^*=2 (B; Re_f=25), t^*=3 (C; Re_f=47.1) and t^*=4 (D; Re_f=50). Between t^*=3 and t^*=4 the flow separates at the top and bottom of the flagellum to form a recirculating flow region containing two vortices downstream of the flagellum.

which ceases to exist at the two points where the flow detaches from the sides of the flagellum.

Figs 6 and 7 provide plots of the calculated profiles for the dimensionless U_x velocity component plotted along two coordinate directions. (Corresponding plots for the U_y velocity component, not provided here, show that, in comparison, it is negligibly small.) Fig. 6 provides the variation of U_x/U_o as a function of x/d_f for y/d_f=10, while Fig. 7 shows the variation of U_x/U_o as a function of y/d_f for x/d_f=5. The results shown are restricted to a subregion of the calculation domain corresponding to the flow of interest, immediately around the flagellum. Relative to the flagellum cylindrical cross-section shown in each figure, in Fig. 6 the flow approaches from the left (creating a stagnation region on the flagellum) and departs from the right (creating a recirculating region immediately behind the flagellum). In Fig. 7 the flow is directed vertically upwards along either side of the flagellum, at locations ±90° downstream of the stagnation point. Velocity profiles are plotted for four dimensionless times, t^*. Also shown for reference in the figures are hypothetical ventral and dorsal (Fig. 6) and medial and lateral (Fig. 7) mechanoreceptor sensilla, of length $0.25\times d_f$ and oriented normal to the flagellum surface. Except for the profiles in the wake of the flagellum (Fig. 6), the gradients of all the other velocity profiles are observed to increase markedly with time near the flagellum surface. In contrast, in the wake region immediately behind the flagellum the U_x velocity component is always relatively small, initially being positive but eventually becoming

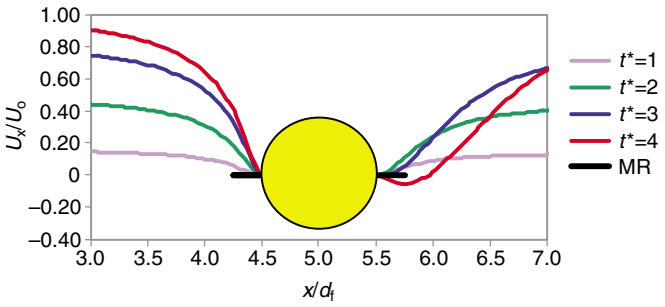

Fig. 6. Profiles of the dimensionless U_x velocity component for the flow approaching (left profiles) and moving away from (right profiles) a flagellum (circle) plotted along the x/d_f axis at y/d_f=10 (passing through the front and back stagnation points of the flagellum). Results are given for four dimensionless times (t^*=1 to t^*=4) for a subregion of the entire $20d_f\times20d_f$ calculation domain, and at t^*=4 the flagellum Reynolds number is Re_f=50. At each time, the U_x velocity component approaching the flagellum drops from the free stream value $U_o(t)$ for that time to the stagnation point value of 0 within less than two flagellum diameters. The region of reversed (negative) flow in the wake of the flagellum grows asymptotically with time (see Fig. 5 also). The black bars denote the lengths, to scale, of $0.25\times d_f$ mechanoreceptor (MR) sensilla oriented normal to the flagellum surface.

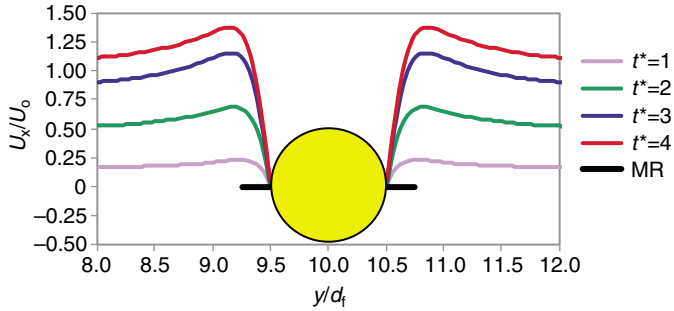

Fig. 7. Profiles of the dimensionless U_x velocity component at locations –90° (left profiles) and + 90° (right profiles) relative to the stagnation point (bottom of circle) for the flow past a flagellum (circle) plotted along the y/d_f axis at x/d_f=5 (passing through the ±90° locations). Results are given for four dimensionless times (t^*=1 to t^*=4) for a subregion of the entire $20d_f\times20d_f$ calculation domain, and at t^*=4 the flagellum Reynolds number is Re_f=50. The symmetrical profiles show the U_x velocity component increasing with time. At each time, the U_x velocity component maximizes near the flagellum surface (a characteristic of this class of flows) and decreases to the free stream value $U_o(t)$ for that time within less than two flagellum diameters. The black bars denote the lengths, to scale, of $0.25\times d_f$ mechanoreceptor (MR) sensilla oriented normal to the flagellum surface.

negative as the wake forms and the flow in it reverses direction. For all times, the medial and lateral mechanoreceptors shown in Fig. 7 remain immersed in the boundary layer.

To a very good approximation, this is the complex transient flow field to which ventral, dorsal, medial and lateral mechanoreceptors are exposed to along the length section $0.50 \leqslant z/L_f \leqslant 0.75$ of a downward-flicking flagellum. However, because of the closeness of the Reynolds numbers the same flow patterns arise for an upward-flicking flagellum, with the sense of motions reversed and their magnitudes decreased, and with the locations of the stagnation and wake flow regions interchanged. As a consequence, fluid motion around a flagellum is such that medial and lateral mechanoreceptor sensilla are torqued in the ventral-to-dorsal direction during a downward flick and in the dorsal-to-ventral direction during an upward flick. Also during a downward flick the ventral sensilla are torqued towards the flagellum surface while the dorsal sensilla are minimally affected. In contrast, during an upward flick it is the dorsal sensilla that are torqued toward the flagellum surface while the ventral are minimally affected. It has been tacitly assumed that the sensilla present on the flagellum (both aesthetascs and putative hydrodynamic mechanoreceptors) do not significantly alter the flow around the flagellum modeled as a cylinder. The assumption is reasonable given the sparseness of the sensilla and their small geometrical dimensions (diameter and length) relative to the flagellum diameter.

(4) Dynamics of the flow around a flagellum in a tube

The FAHTSO code described above was also used to perform numerical calculations of the flow of water at 25°C in a model of the flagellum-in-tube experiment (Mellon and Humphrey, 2007) using the inner dimensions of the experimental tube, length L_t=25 mm and diameter D_t=2.4 mm. Because of the flagellum's small cone angle (3.4°, calculated above), and in order to emphasize the dynamics of the flow in the flagellum length range $0 \leqslant z/L_f \leqslant 0.75$, the flagellum was approximated as a solid rod of length L_f=15 mm and diameter d_f=0.5 mm and was concentrically located in the tube. Two small openings at the ends of the tube and at right angles to it, each of diameter d=1 mm, allowed setting up the proximal-to-distal (P→D) and distal-to-proximal (D→P) flow regimes investigated in the experiments. A schematic of the flow configuration examined, with a definition of the Cartesian coordinate system used for the calculations, is provided in Fig. 8. [Note that the (x, y, z) Cartesian coordinate system used for the flagellum-in-tube calculations is defined so as to coincide with that used for the free-flicking flagellum calculations and, thus, facilitate comparisons between the two sets of results.]

As for the case of the free-flicking flagellum, the flagellum-in-tube calculations were performed on a grid sufficiently refined to accurately capture the geometries of the tube and rod curved surfaces. The grid consisted of 54×54×67 (x, y, z) nodes inside the tube and was unequally refined in order to capture the viscous layers on all solid surfaces. The calculation time step employed was 2×10^{-5} s. At time zero, water motion in the tube was impulsively started from rest by setting a uniform inlet velocity condition at opening A for the P→D flow, or at opening B for the D→P flow, of U_{in}=0.318 m s^{-1} corresponding to a volumetric flow rate through the tube of $\dot{V}$=15 cm^3 min^{-1}=

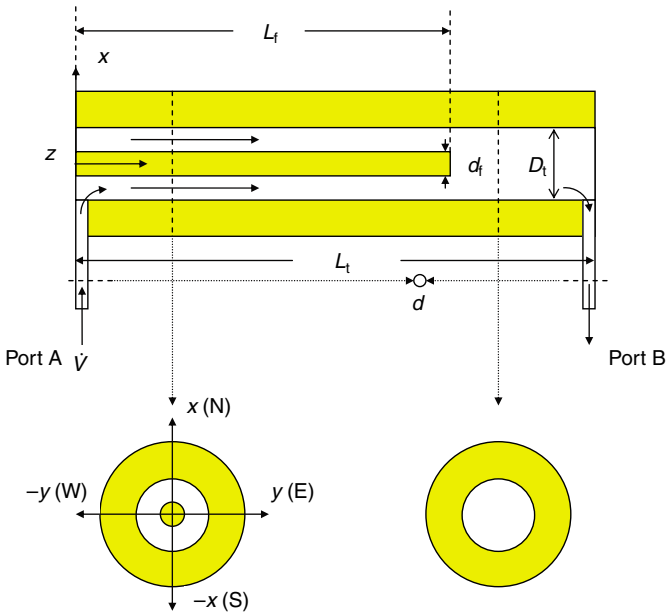

Fig. 8. Schematic (not to scale) of a simplified model of the flagellum-in-tube experiment and definition of the (x, y, z) coordinate system used for plotting the velocity components U_x, U_y and U_z. The case shown corresponds to proximal-to-distal (P→D) flow, entry port A being to the left and exit port B to the right in the figure. Values for the geometrical dimensions and volumetric flow rate are given in the text. N, north; S, south; E, east; W, west.

2.5×10^{-7} m^3 s^{-1}. Because of the larger cross-section of the annular space between the flagellum and the tube, this resulted in an average velocity of $U_{ann}=5.78\times10^{-2}$ m s^{-1} in the annulus. The remaining boundary conditions imposed were: (i) zero velocity at all solid surfaces; (ii) uniform velocity at the outlet opening, equal in magnitude to that at the inlet. For the conditions examined the flow everywhere was always laminar and had essentially developed to its final state by t=0.025 s.

Profiles of the dimensionless U_x, U_y and U_z velocity components in the annular space are provided in Figs 9 and 10 for two typical axial locations in the tube and valid for all times $t \geqslant 0.025$ s. The velocity components are non-dimensionalized using the average velocity in the annulus, U_{ann}, and the x and y coordinates using the tube radius $D_t/2$. A clarification is in order to better understand the discussion below concerning these results and their comparison with the free-flicking flagellum calculations. With reference to Fig. 8, note that in these plots 'S–N' denotes velocity component profiles plotted along the south-to-north compass direction; that is, plotted as a function of x for y=0. Similarly, 'W–E' denotes velocity component profiles plotted along the west-to-east compass direction; that is, plotted as a function of y for x=0.

With reference to Fig. 9, the calculations reveal that the two P→D and D→P flow regimes are virtually the same in magnitude and distribution, but with directions reversed, along the length of the annular space in the range $0.20 \leqslant z/L_t \leqslant 0.60$, approximately. Based on the flagellum length of 15 mm, these values correspond to $0.33 \leqslant z/L_f \leqslant 1$, where the latter position coincides with the tip of the flagellum. In this region the axial velocity, U_z, is the only

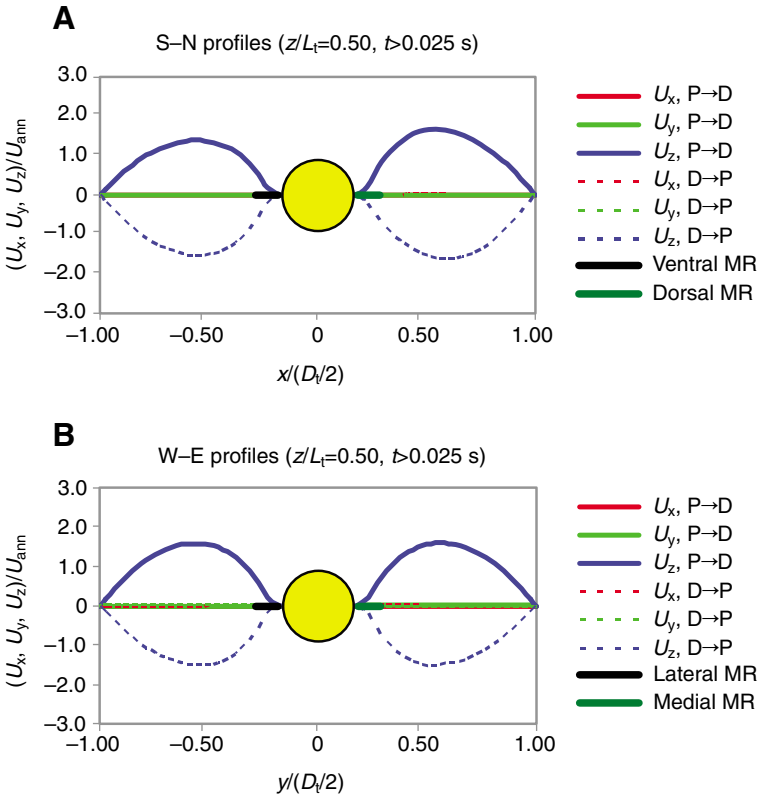

Fig. 9. Dimensionless U_x, U_y and U_z velocity component profiles for the flow in the annular space between a rod-like flagellum and a tube around it along the S–N (A) and W–E (B) compass directions (see Fig. 8). Continuous lines denote velocity profiles corresponding to the P→D flow and broken lines to the D→P flow. Calculation conditions, given in the text, correspond closely to the experimental, and the results shown are typical of the flow in the annular space in the region $0.20 \leqslant z/L_t \leqslant 0.60$ or, equivalently, $0.33 \leqslant z/L_f \leqslant 1$ for times $t \geqslant 0.025$ s. In this region the only significant velocity component is the axial, U_z, which presents the skewed parabolic profile shape characteristic of the developed flow through an annular passage. The black and green bars denote the lengths, to scale, of $0.25 \times d_f$ mechanoreceptor (MR) sensilla oriented normal to the flagellum surface.

significant component of motion and has the skewed parabolic shape characteristic of the developed flow in an annulus.

In contrast, with reference to Fig. 10, between z/L_t=0 and 0.20, corresponding to z/L_f=0 and z/L_f=0.33, the third of the flagellum nearest to its base, the two P→D and D→P flows differ in the following major ways.

P→D flow

The U_z component of motion is relatively large everywhere around the flagellum and of sense such that it torques all mechanoreceptor sensilla towards the flagellum surface. Along the medial and lateral sides of the flagellum (W–E profiles), the U_x component of motion is comparable to U_z and of sense such that it torques medial and lateral sensilla parallel to the flagellum surface and in the ventral-to-dorsal direction. The U_x component of motion in the S–N profiles is of sense such that it also torques dorsal and ventral sensilla towards the flagellum surface while, in contrast, the U_y component in the W–E profiles is of sense such that it torques medial and lateral sensilla away from the flagellum surface. Thus, the U_x component of motion reinforces the torque effects of the U_z when acting on the dorsal and ventral sensilla, but works to neutralize the torque effects of U_z when acting on the medial and lateral sensilla.

D→P flow

The U_z component of motion is comparable to that for the P→D flow everywhere around the flagellum, and of sense such that it torques all sensilla away from the flagellum

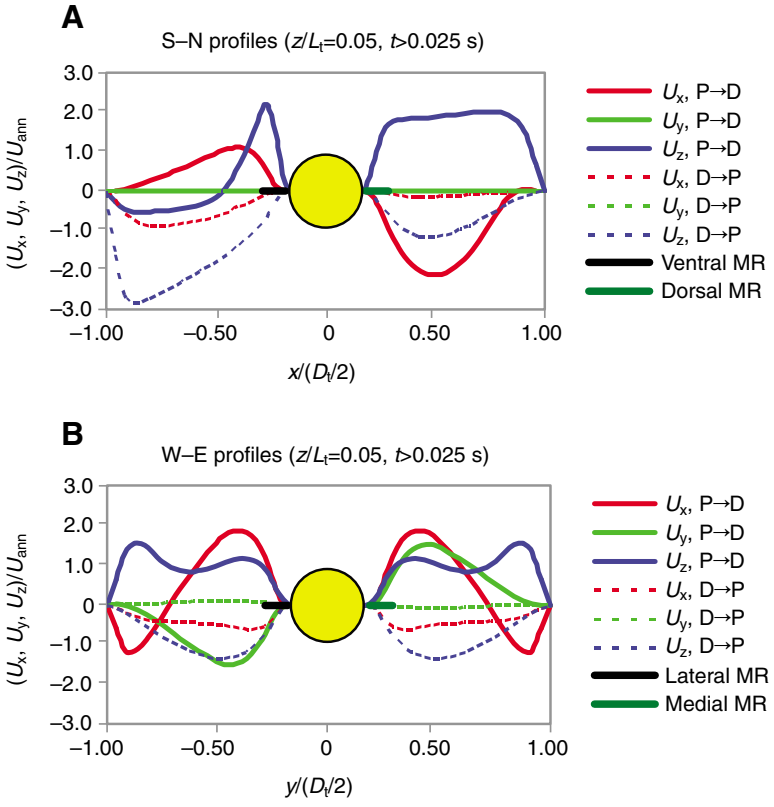

Fig. 10. Dimensionless U_x, U_y and U_z velocity component profiles for the flow in the annular space between a rod-like flagellum and a tube around it along the S→N (A) and W→E (B) compass directions (see Fig. 8). Continuous lines denote velocity profiles corresponding to the P→D flow and broken lines to the D→P flow. Calculation conditions, provided in the text, correspond closely to the experimental, and the results shown are typical of the flow in the annular space in the region $0 \leqslant z/L_t \leqslant 0.20$ or, equivalently, $0 \leqslant z/L_f \leqslant 0.33$ for times $t \geqslant 0.025$ s. In this region the three velocity components are roughly comparable in magnitude, with the P→D flow profiles in the vicinity of the mechanoreceptors corresponding closely to the flow around a downward flicking flagellum and the D→P flow profiles to an upward-flicking flagellum. The black and green bars denote the lengths, to scale, of $0.25 \times d_f$ mechanoreceptor (MR) sensilla oriented normal to the flagellum surface.

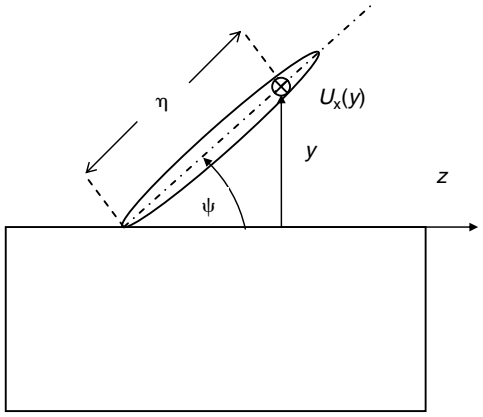

Fig. 11. Schematic, not to scale, for evaluating the drag force and torque acting on a medial or lateral mechanoreceptor sensillum contained in a plane passing through the flagellum axis and oriented at an angle ψ with respect to the local tangent to the flagellum surface. The velocity component, $U_x(y)$, inducing the drag and torque is normal to the plane of the figure and, at any location η along the sensillum, $U_{ns}(\eta)=U_x(y)$ where $y=\eta\sin\psi$.

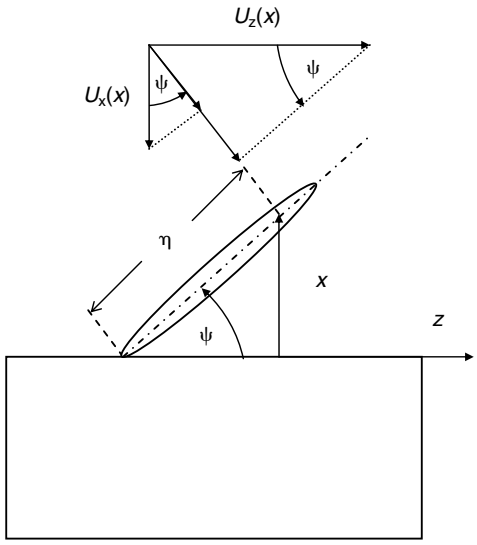

Fig. 12. Schematic, not to scale, for evaluating the drag force and torque acting on a ventral or dorsal mechanoreceptor sensillum contained in a plane passing through the flagellum axis and oriented at an angle ψ with respect to the local tangent to the flagellum surface. The velocity components, $U_x(x)$ and $U_z(x)$, inducing the drag and torque are respectively normal and parallel to the local tangent to the flagellum surface and, at any location η along the sensillum, $U_{ns}(\eta)=U_x(x)\cos\psi+U_z(x)\sin\psi$ where $x=\eta\sin\psi$.

surface. Along the medial and lateral sides of the flagellum (W–E profiles), the U_x component of motion is comparable to the axial and of sense such that it torques medial and lateral sensilla parallel to the flagellum surface and in the dorsal-to-ventral direction. For this case, there are no other significant components of motion affecting the mechanoreceptor sensilla.

From these findings it is clear that, over the length $0\leqslant z/L_f\leqslant 0.33$ of the 15 mm flagellum section in the tube, the P→D flow closely mimics the motion past a flagellum during a downward-directed flick and, in so far as the medial and lateral mechanoreceptor sensilla are concerned, the D→P flow closely mimics the motion corresponding to an upward-directed flick. (An even closer correspondence would be attained between the D→P flow and an upward-directed flick if the axial flow worked to torque the sensilla toward the flagellum surface, as in the P→D flow case, as opposed to away from the flagellum surface.) For the flagellum length corresponding to $0.33\leqslant z/L_f\leqslant 1$, the P→D and D→P flows in the annular space are strictly axially directed, equal in magnitude and distribution, but of opposite sense. Along this section of the flagellum, all sensilla experience the same torque magnitude but with sense dictated by the axial flow direction. The main conclusions are that: (i) the P→D flow in the tube torques all mechanoreceptor sensilla towards the flagellum surface and the medial and lateral in the ventral-to-dorsal direction; (ii) the D→P flow torques all sensilla away from the flagellum surface and the medial and lateral in the dorsal-to-ventral direction. The first situation corresponds closely to that expected for a downward-flicking flagellum, while the second corresponds well, but to a lesser degree, to that expected for an upward-flicking flagellum.

(5) Drag forces and torques acting on the hydrodynamic mechanoreceptor sensilla of free-flicking and tube flow flagella

The putative hydrodynamic mechanoreceptor sensilla of interest have slightly curved beak-like shapes at their tips and, as a consequence, are also referred to as 'beaked' sensilla in the text. They are arrayed around the circumference of each annular segment of the flagellum (dorsally, ventrally, medially and laterally) and vary in length from 50 to 250 μm with diameters ranging from 10 μm at the base to 2 μm at the tip. These sensilla point distally along the flagellum, each being contained in a plane that passes through the local flagellum axis, and they have orientation angles, ψ, measured with respect to the tangent to the flagellum surface (see Fig. 2), ranging from 35° to 65°.

In this study we are concerned with the drag forces and torques acting on these sensilla modeled as straight, truncated cylinders of diameter d_{MR}=10 μm, length L_{MR}=125 μm, and orientation angle ψ=45°. For the purposes of an analysis based on the fluid mechanics results presented in the sections above, in the case of a flicking flagellum attention is restricted to representative sensilla located in the range $0.50\leqslant z/L_f\leqslant 0.75$ of a 25 mm flagellum of diameter very close to d_f=0.5 mm in this range. In the case of the flagellum in a tube, we are primarily concerned with representative sensilla in the range $0\leqslant z/L_f\leqslant 0.33$ of a flagellum 15 mm long with diameter d_f=0.5 mm, for which the experiment closely mimics downward and upward free-flicking flagellum conditions.

The velocity distributions obtained for a free-flicking flagellum and for a flagellum in the tube flow configuration corresponding to the experiment, allow estimations of the drag forces and torques acting upon the hydrodynamic mechanoreceptors distributed circumferentially around a segment of the flagellum. Since certain characteristics of the mechanoreceptors such as their torsional restoring constants

and damping constants are currently unknown, attention is paid to estimating the maximum drag forces and torques they can possibly experience. To this end, it is assumed that the sensilla are rigidly fixed (do not move relative to the flagellum) and are inflexible (do not bend). We know the latter assumption is correct from Atomic Force Microscope (AFM) experiments performed by others (H. C. Jennings and E. Berger, personal communication). They find that the application of a force, using an AFM tip at different locations along the length of a beaked-shape *Procambarus* antennular sensillum, deflects the entire sensillum without bending it. The former assumption allows us to obtain maximum estimates of the drag and torque, which are of the correct order of magnitude for a deflecting mechanoreceptor.

With reference to Fig. 2, which defines the velocity component U_{ns} normal to a sensillum, it is easy to verify that the characteristic Reynolds number, $Re_{MR}[\equiv (d_{MR}U_{ns}\rho)/\mu]$, for the flow around a hydrodynamic mechanoreceptor, whether on a free-flicking flagellum or the flagellum-in-tube experiment, is $Re_{MR}\leqslant 1$. Because, in addition, $L_{MR}/d_{MR}\geqslant 1$, the Oseen drag relation for the flow past a cylinder can be used to calculate the instantaneous drag force per unit length, f_{MR}, acting on the sensillum. The relation, available in White (White, 1974) and adapted to the present work, is given by:

$$f_{MR} = \frac{1}{2}\rho U_{ns}^2 d_{MR}\,\frac{8\pi}{Re_{MR}[0.5-\Gamma+\ln(8/Re_{MR})]}\,, \qquad (2)$$

where Γ=0.577216 is Euler's constant. It follows that the total drag force acting on a sensillum is given by:

$$F_{MR} = \int_0^{L_{MR}} f_{MR}\,d\eta\,, \qquad (3)$$

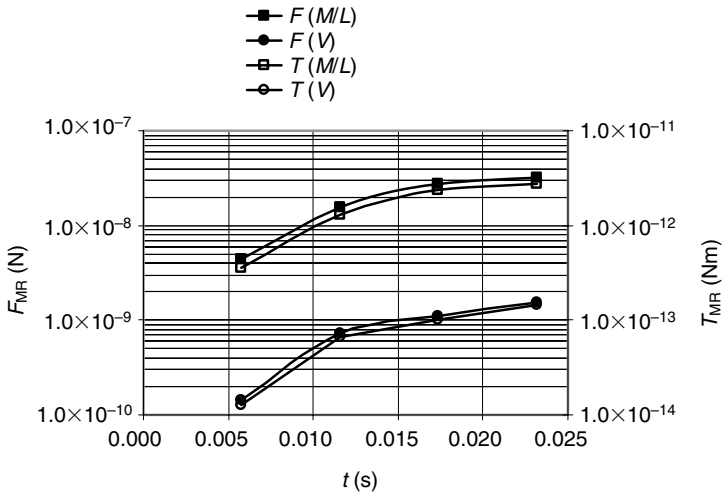

Fig. 13. Maximum values of the drag forces (F_{MR}, N) and torques (T_{MR}, Nm) acting on the medial and lateral (M/L) and ventral (V) mechanoreceptor sensilla of a downward flicking flagellum calculated as a function of time. Calculation conditions and methodology are given in the text.

and the corresponding torque by:

$$T_{MR} = \int_0^{L_{MR}} f_{MR}\,\eta\,d\eta\,, \qquad (4)$$

where η is the distance along the length of the sensillum.

Note that because both the flows of interest accelerate with time, in principle an added mass term of order $f_{AM}=\rho\pi(d_{MR}/2)^2(dU_{ns}/dt)$ contributes to the force per unit length acting on a mechanoreceptor. It is easy to show that:

$$\frac{f_{AM}}{f_{MR}} = \frac{\pi d_{MR}}{2}\,\frac{(dU_{ns}/dt)}{U_{ns}^2}\,\frac{Re_{MR}[0.5-\Gamma+\ln(8/Re_{MR})]}{8\pi}\,, \qquad (5)$$

Table 1. *Summary and comparison of the calculated maximum drag forces and torques acting on the mechanoreceptor sensilla of a free-flicking flagellum and a flagellum-in-tube flow case*

	Calculated maximum drag forces (N) and torques (Nm) acting on flagella hydrodynamic mechanoreceptor sensilla	
Free-flicking flagellum (sensilla in the range $0.50\leqslant z/L_f\leqslant 0.75$)	Downward flick	Upward flick
Ventral sensillum	$F_{MR}=1.56\times10^{-9}$, $T_{MR}=1.45\times10^{-13}$ (directed toward flagellum surface)	(very small relative to downward flick values)
Dorsal sensillum	(very small relative to upward flick values)	$F_{MR}=7.8\times10^{-10}$, $T_{MR}=7.25\times10^{-14}$ (directed toward flagellum surface)
Medial/lateral sensilla	$F_{MR}=3.17\times10^{-8}$, $T_{MR}=2.72\times10^{-12}$ (directed ventral-to-dorsal)	$F_{MR}=1.59\times10^{-8}$, $T_{MR}=1.36\times10^{-12}$ (directed dorsal-to-ventral)
Flagellum in tube (sensilla in the range $0\leqslant z/L_f\leqslant 0.33$)	P→D flow (analog of downward flick)	D→P flow (analog of upward flick)
Ventral/dorsal sensilla	$F_{MR}=6.63\times10^{-9}$, $T_{MR}=6.45\times10^{-13}$ (directed toward flagellum surface)	$F_{MR}=5.98\times10^{-10}$, $T_{MR}=5.75\times10^{-14}$ (directed away from flagellum surface)
Medial/lateral sensilla	$F_{MR}=7.12\times10^{-9}$, $T_{MR}=6.47\times10^{-13}$ (directed ventral-to-dorsal)	$F_{MR}=3.36\times10^{-9}$, $T_{MR}=3.02\times10^{-13}$ (directed dorsal-to-ventral)

F, force; *T*, torque; MR, mechanoreceptor.

The table results apply for all times $t>0.023$ s for a free-flicking flagellum and $t>0.025$ s for the flagellum-in-tube flow case. For calculation conditions and methodology, see text.

and, using the data leading to the plots in Figs 6 and 7, we find that $f_{AM}/f_{MR} \leqslant 0.1$ for times $t^* \geqslant 1$ ($t \geqslant 5.79\times10^{-3}$ s). For times $t^* \leqslant 0.1$ ($t \leqslant 5.79\times10^{-4}$ s) we find that $f_{AM}/f_{MR} \geqslant 10$, but f_{MR} is so small at such early times as to render both itself and f_{AM} negligible. Thus in our analyses we neglect the contribution of the added mass to the force and torque acting on a mechanoreceptor.

In applying Eqn 3 and Eqn 4, care must be taken to evaluate U_{ns} correctly along the length, η, of the sensillum. With reference to Fig. 11, for a medial or lateral sensillum it is easy to show that $U_{ns}(\eta)=U_x(y)$, the component of motion normal to the plane of the figure, where $y=\eta\sin\psi$. For a free-flicking flagellum $U_x(y)$ is obtained from the data used to generate Fig. 7, and for the flagellum-in-tube flow case $U_x(y)$ is obtained from the data used to generate the W–E profiles in Fig. 10. Fig. 12 shows the most general situation for a ventral sensillum during a downward flick (or a dorsal one during an upward flick). Now $U_{ns}(\eta)=U_x(x)\cos\psi+U_z(x)\sin\psi$, where $x=\sin\psi$. In the z/L_f range of interest here for a free-flicking flagellum $U_z(x)=0$ so that $U_{ns}(\eta)=U_x(x)\cos\psi$ and, in this case, $U_x(x)$ is obtained from the data used to generate Fig. 6. In the z/L_f range considered for the flagellum-in-tube case, particularly the P→D flow, both $U_x(x)$ and $U_z(x)$ can contribute to $U_{ns}(\eta)$ and their values are obtained from the data used to generate the S–N profiles in Fig. 10.

Fig. 13 shows the time variation of the calculated drag forces and torques acting on the medial, lateral and ventral mechanoreceptor sensilla of a downward-flicking flagellum ultimately attaining a final, developed flow Reynolds number of $Re_f=50$. The plots reveal two distinct trends: (i) the total drag forces and torques for all these sensilla increase to asymptotic values associated with the developed flow condition attained by the flagellum by $t^*=4$ ($t=0.023$ s); (ii) at any time, the drag forces and torques acting on the medial and lateral sensilla are 20–30 times larger than the corresponding forces/torques acting on the ventral sensilla.

Corresponding results for the drag forces and torques acting on the medial, lateral and dorsal sensilla of an upward-flicking flagellum (not plotted in Fig. 13) show exactly the same trends but are half as large in numerical value because of the smaller upward-flick velocity. That this should be the case is readily proven using Eqn 2 to obtain the ratio of the forces per unit length acting on a mechanoreceptor during an upward and downward flick, respectively. The ratio is given by:

$$\frac{f^{U}_{MR}}{f^{D}_{MR}} = \frac{U^{U}_{ns}}{U^{D}_{ns}} \times \frac{[0.5–\Gamma+\ln(8/Re^{D}_{MR})]}{[0.5–\Gamma+\ln(8/Re^{U}_{MR})]} \ , \qquad (6)$$

where superscripts U and D denote upward and downward flick conditions, respectively. A numerical evaluation of the second term on the right hand side of Eqn 6 yields a value of 0.85±0.03 over the range of values for Re_{MR} of this study. Since we also know that $U^{U}_{ns}/U^{D}_{ns} \approx 0.6$ it follows that $f^{U}_{MR}/f^{D}_{MR} \approx 0.51\pm0.02$.

Table 1 summarizes and compares the sensilla drag and torque results obtained for a downward and upward free-flicking flagellum, and for the flagellum-in-tube configuration. The values in the table for the flicking flagellum correspond to $t \geqslant 0.023$ s ($t^* \geqslant 4$), while those for the flagellum-in-tube configuration correspond to $t \geqslant 0.025$ s. The tabulated values reveal three trends. Relative to corresponding values obtained for a downward and upward flicking flagellum, in the flagellum-in-tube configuration: (i) ventral (dorsal) sensilla experience drag forces and torques that are about 4.3 times larger (1.3 times smaller) for the P→D flow (for the D→P flow); (ii) medial and lateral sensilla experience drag forces and torques that are about 4.5 times smaller for the P→D flow and 4.7 times smaller for the D→P flow; (iii) as for the free-flicking flagellum, drag forces and torques are about 2 times larger for the P→D flow than for the D→P flow.

The conclusions are that, for times $t > 0.025$ s: (i) the flagellum-in-tube experiment yields values of drag forces and torques acting on the flagellum sensilla that are well within the range of the values experienced by a free-flicking flagellum for both downward and upward flicking conditions; (ii) the P→D flow induces larger values of the drag forces and torques acting on the sensilla than the D→P flow, showing good correspondence with the downward and upward flicks of a free-flicking flagellum.

The authors thank Dr W. O. Friesen for his assistance and expertise in performing kinematic observations of a flicking crayfish flagellum, and Dr C. Barbier and Dr A. Pillapakam for their assistance in performing the flagellum-in-tube and free-flicking flagellum flow calculations, respectively. Thanks also go to Mr H. C. Jennings and Dr E. Berger for permitting the reference to their unpublished data. J.A.C.H. wishes to acknowledge partial support provided through a DARPA BioSenSE AFOSR award (Grant # FA9550-05-1-0459) during the performance of this study.

References

Mellon, DeF. and Humphrey, J. A. C. (2007). Directional asymmetry in responses of local interneurons in the crayfish deutocerebrum to hydrodynamic stimulation of the lateral antennular flagellum: experimental findings and theoretical predictions. *J. Exp. Biol.* **210**, 2961-2968.

Panton, R. L. (1996). *Incompressible Flow*. New York: John Wiley.

Pillapakkam, S. B., Barbier, C., Humphrey, J. A. C., Rüter, A., Otto, B., Bleckmann, H. and Hanke, W. (2007). Experimental and numerical investigation of a fish artificial lateral line canal. In *Proceedings of the 5th International Symposium on Turbulence and Shear Flow Phenomena* (ed. R. Friedrich, N. A. Adams, J. K. Eaton, J. A. C. Humphrey, N. Kasagi and M. A. Leschziner), vol. 3, pp. 1017-1022.

Rosales, J. L., Ortega, A. and Humphrey, J. A. C. (2000). A numerical investigation of the convective heat transfer in unsteady laminar flow past a single and tandem pair of square cylinders in a channel. *Num. Heat Transfer A* **38**, 443-465.

Rosales, J. L., Ortega, A. and Humphrey, J. A. C. (2001). A numerical simulation of the convective heat transfer in confined channel flow past square cylinders: comparison of inline and offset tandem pairs. *Int. J. Heat Mass Transfer* **44**, 587-603.

Tritton, D. J. (1988). *Physical Fluid Dynamics*. Oxford: Clarendon Press.

White, F. M. (1974). *Viscous Fluid Flow*. New York: McGraw-Hill.